Journal of Computational Mathematics
Vol.28, No.3, 2010, 401–417.

http://www.global-sci.org/jcm
doi:10.4208/jcm.2009.10-m2873

ACCURATE ATTENUATION CORRECTION FOR ALGEBRAIC RECONSTRUCTION TECHNIQUE IN SPECT*

Elie Nasr
IMB, Institute of Mathematics of Bordeaux, UMR 5251, Université Bordeaux 1, 351, Cours de la Libration - 33405 Talence, France
Email: elienasr@usek.edu.lb

Abstract

We present a new iterative reconstruction algorithm to improve the algebraic reconstruction technique (ART) for the Single-Photon Emission Computed Tomography. Our method is a generalization of the Kaczmarz iterative algorithm for solving linear systems of equations and introduces exact and implicit attenuation correction derived from the attenuated Radon transform operator at each step of the algorithm. The performances of the presented algorithm have been tested upon various numerical experiments in presence of both strongly non-uniform attenuation and incomplete measurements data. We also tested the ability of our algorithm to handle moderate noisy data. Simulation studies demonstrate that the proposed method has a significant improvement in the quality of reconstructed images over ART. Moreover, convergence speed was improved and stability was established, facing noisy data, once we incorporate filtration procedure in our algorithm.

Mathematics subject classification: 65F10, 65R32, 68U10, 92C55.
Key words: Single-photon emission computed tomography, Attenuated radon transform, Algebraic reconstruction technique, Attenuation correction.

1. Introduction

1.1. The medical aspect

Single-Photon Emission Computed Tomography (SPECT) is a nuclear medical imaging mechanism used to determine the concentration of some biologically active molecules in some specific zone of a human body in terms of their activity distribution. Some radiopharmaceutical product is first injected into the patient's organ, with a Gamma-emitting isotope. The radiations are trapped by a Gamma-camera with detectors which is materialized by an acquisition plane, see Fig. 1.1, rotating about the patient along a grid of specific angles. The intensity of such radiations is therefore measured in each direction orthogonal to the acquisition system plane in various angular positions.

The measured quantities of traveling photons are the exponentially weighted averages of the activity distribution along straight lines on their way from the source to the detector. The reason for the exponential weight is the presence of a position-dependent attenuation coefficient (see [12]) due to photon interaction with the organic tissue in which the radiations go through.

* Received July 21, 2008 / Revised version received September 16, 2008 / Accepted October 20, 2009 / Published online February 1, 2010 /

1.2. The mathematical model

We will present here a two-dimensional model, so that the detector will be materialized by a grid of collimators regularly spaced along a line C which modelizes the Gamma-camera. Let $(x,y) \longmapsto f(x,y)$ denote the activity distribution and $(x,y) \longmapsto a(x,y)$ the position-dependent attenuation coefficient. When the detector is positioned in order to register radiations which propagate along lines L with direction $\theta^\perp$, the measured intensity $g(\theta,\ s(L))$ corresponding to the radiation along such line distant from $s = s(L)$ to the origin (the center of the exploration zone) (see Figs. 1.1a and 1.1b), is given by the attenuated Radon transform $(\theta, s) \longmapsto R_{a,\ \theta}[f](s)$ defined as :

$$\begin{aligned} R_{a,\theta}\ [f](s) &= \int_{\langle (x,y),\ \theta\rangle = s} \exp\Big(- \int_0^{+\infty} a((x,y) + t\theta^\perp)\, dt\Big)\, f(x,y)\, d\lambda_{s,\theta}(x,y) \\ &= g(\theta,\ s). \end{aligned} \tag{1.1}$$

Here $d\lambda_{s,\theta}$ stands for the restriction of the Lebesgue area measure in $\mathbb{R}^2$ to the straight line $\langle (x,y)\,,\, \theta\rangle = s$, where

$$\theta = \begin{pmatrix} \cos\varphi \\ \sin\varphi \end{pmatrix}, \quad \theta^\perp = \begin{pmatrix} -\sin\varphi \\ \cos\varphi \end{pmatrix} \quad \text{and} \quad 0 \le \theta < \varphi_{\max}.$$

The unknown activity distribution is materialized in (1.1) by f. So the problem is to recover f from the projections data $g(\theta,\ s)$, assuming of course some *a priori* information about the tissue attenuation distribution a. When a is known, there are various direct (*via* analytic formulas) or iterative techniques to recover f.

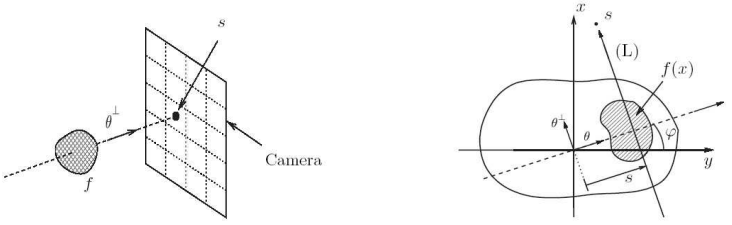

(a) (b)

Fig. 1.1. Scanner

1.3. Previous inversion methods

Direct analytic methods lie on explicit exact inversion formulas for the attenuated Radon transform. When $a \equiv 0$, the problem is solved by the classical Radon inversion formulas in dimension two (see Natterer [15] and Quinto [18] for more details about Radon's inversion formulas). When the attenuation tissue distribution a remains constant on the support of f, then the attenuated Radon transform is reduced to the exponential Radon transform, for which Tretiak and Metz [23] suggested an exact inversion formula. Nevertheless, none of these analytical methods is accurate respect to the reconstruction of f in case of an arbitrary strongly non-uniform attenuation tissue distribution, which is usually the case in any realistic SPECT problem. Novikov [17] discovered an exact analytical inversion formula for the attenuated Radon transform when a is an arbitrary tissue attenuation distribution. Another derivation of

a similar formula and numerical inversion were developed by Natterer [16]. See also [13] for numerical applications.

On the other hand, there is a wide family of iterative methods involving linear algebra, operator theory and statistical tools. One of the prominent iterative reconstruction methods for emission tomography is Maximum Likelihood Reconstruction using the EM algorithm, which stands for Expectation Maximization presented by Dempster *et. al* [5] in its full generality. A practical implementation of the EM method in the setting of image reconstruction was proposed by Shepp and Vardi [21], where a statistical framework for the problem is given. However, classical EM algorithm, in itself, does not take into account the attenuation correction. Many studies have been made to incorporate attenuation correction procedure in the main EM algorithm. Tsui *et. al* [24] implemented an iterative EM algorithm with attenuation correction using an attenuated projector-backprojector that uses the attenuation distribution to calculate attenuation factors for each pixel along each projection and backprojection. See also [1] for similar studies. A fast EM algorithm for image reconstruction from the attenuated projections with Poisson noise was proposed in [9].

Some of the iterative algorithms involve evaluation of certain analytic formulas as a part of the method. A multiplicative postprocessing technique was implemented by Chang [3] for attenuation correction using an assumed constant attenuation coefficient. This technique was modified to calculate the multiplicative attenuation compensation factor, based on a nonuniform attenuation distribution, and combined iteratively with the filtered backprojection algorithm. See Manglos *et. al* [14].

With the condition $a = 0$, there is a well known iterative method to solve (1.1) in order to recover f from its projection $g(\theta, s)$ with no attenuation correction. This method is known as Algebraic Reconstruction Technique and commonly denoted by ART. it is based on the well known algorithm for solving linear systems of equations proposed by Kaczmarz in 1937 cite11 and later elucidated further by Tanabe [22]. The application of the ART in tomography was introduced by Gordon *et. al* [7] in 1970. Later Herman [8] showed that ART can be computationally efficient by carefully arranging the order in which the collected data are accessed during the iterative reconstruction procedure, and by adaptively adjusting the relaxation parameters. ART consists in assuming that the activity distribution f is an array of unknowns, then setting (1.1) as a system of algebraic equations for the unknowns in terms of the measured projection data, and finally applying Kaczmarz method to solve the latter system. The classical ART does not take into account the attenuation of the photons. In [4], Chen *et. al* proposed a method for attenuation correction and combined it with the classical ART algorithm. However their method was based on relation of attenuation coefficient and emission coefficient, which is not always available in realistic models.

1.4. Plan of the article

In this paper we present an iterative reconstruction algorithm with implicit attenuation correction. Our approach is a generalization of the classical ART algorithm. The paper is organized as follows. In section 2 we review the general Kaczmarz method. In section 3 we apply this method to solve the equation (1.1) and derive our iterative algorithm. The main idea of our approach is based on expressing the attenuated Radon transform operator $R_{a,\theta}$ as the decomposition of the Radon transform operator R_θ and a multiplication operator $L_{a,\theta}$. This leads to find an exact and implicit expression for the attenuation correction in the iterative algorithm. In section 4 we illustrate various numerical tests performed with both optimal

and suboptimal data measurements using the present algorithm and the conventional ART algorithm. These tests were done with several activity distribution phantoms and realistic strongly nonuniform attenuation distribution. From this experiments one can see that an algorithm that would not take into account the attenuation would be essentially inaccurate, while our method significantly improves reconstruction results and accelerate convergence speed. We also include in this section reconstruction from noisy data using a filtered version of our algorithm. Finally, section 5 concludes our paper with discussions and comments.

2. Kaczmarz's Method

Kaczmarz's method is an iterative method for solving linear systems of equations. In this section we will present a brief analysis of this method independently of computerized tomography. This analysis will provide the theoretical support needed to compute the algorithm for reconstruction of the activity distribution f from the emission data $R_a[f]$ with a known tissue attenuation distribution a.

Let H and H_j for $j = 1, \ldots, p$ be real (or complex) Hilbert spaces, and let

$$R_j : H \longrightarrow H_j \text{ for } j = 1, \ldots, p$$

be p linear continuous maps from H onto H_j. Let also $g_j \in H_j$ be given and suppose one wants to compute $f \in H$ such that

$$R_j f = g_j \text{ for } j = 1, \ldots, p. \tag{2.1}$$

This linear system can also be written as $Rf = g$, with

$$R = \begin{pmatrix} R_1 \\ \vdots \\ R_p \end{pmatrix}, \quad g = \begin{pmatrix} g_1 \\ \vdots \\ g_p \end{pmatrix} \quad \text{for } j = 1, \ldots, p.$$

Let P_j be the orthogonal projection in H onto the affine subspace

$$\{f \in H \,;\, R_j f = g_j\}$$

with underlying vectorial subspace

$$F_j = \operatorname{Ker} R_j \,.$$

We define the following operators such that

$$P_j^\omega = (1-\omega)I + \omega P_j, \quad P^\omega = P_p^\omega \circ \ \ldots \ \circ P_1^\omega,$$

where ω is a relaxation parameter.

Then, Kaczmarz's method with relaxation for the solution of the equation (2.1) is based on the following inductive computation

$$f_k = P^\omega f_{k-1} \quad \text{for } k = 1, 2, \ldots \tag{2.2}$$

starting with f_0 as an arbitrary initial guess. For $\omega = 1$, we have the classical Kaczmarz's method. Its geometric interpretation is obvious. In fact starting with f_0, we compute f_1 by successive orthogonal projections of f_0 onto the affine subspaces $\{f \,;\, R_j f = g_j\}$ for $j = 1, \ldots, p$.

In order to obtain f_2, we apply the same process to f_1, and so on to reach the kth iteration of the algorithm.

Bellow we are going to give an explicit form for the equation (2.2) by evaluating $P_j f$ for a given $f \in H$. We suppose that the operators R_j for $j = 1, \ldots, p$, are surjective. Hence their adjoint operators $R_j^* : H_j \longrightarrow H$ are injective. Also the operators $R_j \circ R_j^*$ for $j = 1, \ldots, p$, are injective since

$$\langle R_j \circ R_j^*[u]\,,\, u\rangle = \|R_j^*[u]\|^2 \quad \text{for any } u \in H_j.$$

Assuming in addition that all operators $R_j \circ R_j^*$ for $j = 1, \ldots, p$, have closed range, we conclude that

$$R_j \circ R_j^* : H_j \longrightarrow H_j\,, \text{ for } j = 1, \ldots, p\,,$$

is bijective with a continuous inverse $(R_j \circ R_j^*)^{-1}$.

One has

$$(\operatorname{Ker} R_j)^{\perp} = \overline{\operatorname{Im} R_j^*}\,, \text{ for } j = 1, \ldots, p\,,$$

which implies that for each $j = 1, \ldots, p$, there exists a sequence $(u_{j,l}(f))_l \in H_j$ such that

$$P_j f - f = \lim_{l \to +\infty} (R_j^*[u_{j,l}(f)])\,, \quad \text{for } j = 1, \ldots, p\,. \tag{2.3}$$

On the other hand we have $R_j[P_j f] = g_j$, for $j = 1, \ldots, p$, which leads by applying R_j on both sides of (2.3), to

$$g_j - R_j f = \lim_{l \to \infty} [R_j \circ R_j^*(u_{j,l}(f))]\,. \tag{2.4}$$

Once applying the operator $[R_j \circ R_j^*]^{-1} : H_j \longrightarrow H_j$, we see that the sequence $(u_{j,l}(f))_l$ converges to $(R_j \circ R_j^*)^{-1}(g_j - R_j f)$. Consequently,

$$P_j f = f + R_j^*\Big[(R_j \circ R_j^*)^{-1}(g_j - R_j f)\Big]\,, \quad \text{for } j = 1, \ldots, p\,. \tag{2.5}$$

This gives an alternative form to (2.2) and tells us how to compute f_{k+1} from f_k. Therefore, the iterative algorithm of Kaczmarz stands as

$$\begin{aligned} &f_{k,0} = f_k,\\ &f_{k,j} = P_j^{\omega}\, f_{k,j-1} = f_{k,j-1} + \omega\Big[R_j^* \circ \big[R_j \circ R_j^*\big]^{-1}\big(g_j - R_j\, f_{k,j-1}\big)\Big],\ \ 1 \le j \le p\\ &f_{k+1,0} = f_{k,p}, \end{aligned} \tag{2.6}$$

with the initial condition $f_0 = f_{0,0}$.

3. Derivation of the Algorithm

In this section we adapt Kaczmarz's iterative method to the tomographic problem which consists in the inversion of the attenuated Radon transform and the retrieval of the unknown source f from its attenuated projections defined in (1.1) when the attenuation tissue distribution a is known. Since we are dealing with the reconstruction of cross sections of the human body, we will only treat the bi-dimensional case.

In this setting, H is the following space

$$H = L^2_{\mathbb{C}}\Big(\overline{D(0,1)}, dxdy\Big)$$

of mesurable image-functions in the unit closed disc $\overline{D(0,1)}$ of $\mathbb{R}^2$, equipped with the area Lebesgue measure $dxdy$.

Let a be a "sufficiently smooth", say at least continuous, complex valued function in $\overline{D(0,1)}$

$$a: \ \overline{D(0,1)} \longmapsto \mathbb{C}\,,$$

which modelizes the known tissue attenuation distribution of a cross-section body materialized by $\overline{D(0,1)}$. For $\theta \in [0, 2\pi[$, we define the following operator

$$R_{a,\theta}: \ H \longrightarrow h := L^2_{\mathbb{C}}\Big([-1,1], \frac{ds}{\sqrt{1-s^2}}\Big),$$

where $R_{a,\theta}$ is represented by the almost everywhere defined function in $[-1,1]$ with finite energy

$$s \longmapsto \int_{\langle (x,y),\theta\rangle = s} \exp\Big(-\int_0^{+\infty} a((x,y)+t\theta^{\perp})\,dt\Big)\, I(x,y)\, d\lambda_{s,\theta}(x,y)\,,$$

and $d\lambda_{s,\theta}$ stands for the restriction of the Lebesgue area measure in $\mathbb{R}^2$ to the line

$$\Big\{(x,y) \in \mathbb{R}^2\,;\, \langle (x,y),\theta\rangle = s\Big\}\,.$$

The operator $R_{a,\theta}$ can be written as the composition $R_\theta \circ L_{a,\theta}$, where $L_{a,\theta} \ : \ H \longrightarrow H$ is the multiplication operator by the following continuous function

$$\mathrm{A}_{a,\theta} \ : (x,y) \longmapsto \exp\Big(-\int_0^{+\infty} a((x,y)+t\theta^{\perp})\,dt\Big) \tag{3.1}$$

and $R_\theta \ : H \longrightarrow h$ is the Radon $f \longmapsto R[f](\theta,\cdot)$ operator which assigns to f the function

$$s \longmapsto \int_{\{\langle (x,y),\theta\rangle = s\}} f(x,y)\, d\lambda_{s,\theta}(x,y)\,.$$

Thus $R_{a,\theta} = R_\theta \circ L_{a,\theta}$ is surjective since R_θ is surjective. the adjoint operator of $R_{a,\theta}$ is

$$R^*_{a,\theta} = L^*_{a,\theta} \circ R^*_\theta\,,$$

where $L^*_{a,\theta}$ is the adjoint operator of $L_{a,\theta}$ defined by the multiplication operator by the continuous function $\overline{\mathrm{A}_{a,\theta}}$, and $R^*_{a,\theta}$ is the adjoint operator of R_θ. We have (see Natterer [15], p. 18)

$$\begin{array}{rccl} R^*_\theta: & h & \longmapsto & H, \\ & g & \longmapsto & \Big((x,y) \longmapsto \Big[\dfrac{g}{\sqrt{1-s^2}}\Big]_{s=\langle (x,y)\,,\,\theta\rangle}\Big)\,, \end{array}$$

and $R_\theta \circ R^*_\theta = 2\mathrm{Id}_h$ (see Natterer [15], p. 144) since

$$\begin{aligned} R_\theta \circ R^*_\theta\,[g](s) &= \int_{\{\langle (x,y)\,,\,\theta\rangle = s\}} \Big(\frac{g(s)}{\sqrt{1-s^2}}\Big)\, d\lambda_{s,\theta}(x,y) \\ &= \frac{g(s)}{\sqrt{1-s^2}} \times (2\sqrt{1-s^2}) = 2g(s)\,. \end{aligned} \tag{3.2}$$

Therefore, the operator

$$R_{a,\theta} \circ R^*_{a,\theta} = R_\theta \circ L_{a,\theta} \circ L^*_{a,\theta} \circ R^*_\theta$$

is the operator which maps the function $g \in h$ into the following one

$$\begin{aligned} s \longmapsto & \int_{\{\langle (x,y)\,,\,\theta\rangle = s\}} \frac{g(s)}{\sqrt{1-s^2}}\, |\mathrm{A}_{a,\theta}(x,y)|^2\, d\lambda_{s,\theta}(x,y) \\ = & \frac{g(s)}{\sqrt{1-s^2}} \int_{\{\langle (x,y)\,,\,\theta\rangle = s\}} |\mathrm{A}_{a,\theta}(x,y)|^2\, d\lambda_{s,\theta}(x,y) \\ = & \frac{g(s)}{\sqrt{1-s^2}} \int_{-\sqrt{1-s^2}}^{\sqrt{1-s^2}} \exp\Big[-2\mathrm{Re}\Big(\int_{\{0\le\xi\le\sqrt{1-s^2}-t\}} a(s\,\theta + (t+\xi)\theta^\perp)\, d\xi\Big)\Big]\, dt\,. \end{aligned}$$

As we notice, $R_{a,\theta} \circ R^*_{a,\theta}$ is the multiplication operator by the strictly positive bounded function $B_{a,\theta}$ defined by

$$\begin{aligned} s \in [-1,1] \longmapsto & \frac{\displaystyle\int_{-\sqrt{1-s^2}}^{\sqrt{1-s^2}} \exp\Big[-2\mathrm{Re}\Big(\int_{\{0\le\xi\le\sqrt{1-s^2}-t\}} a(s\,\theta + (t+\xi)\theta^\perp)\, d\xi\Big)\Big]\, dt}{\sqrt{1-s^2}} \\ = & \frac{R_\theta\big[|A_{a,\theta}|^2\big]}{\sqrt{1-s^2}}\ . \end{aligned}$$

Such a multiplication operator is a continuous invertible operator of the space h in itself.

Consider distinct angles $\theta_j \in [0, 2\pi[$ with $j = 1,\ \ldots,\ p$, and p vectors $g_1,\ \ldots,\ g_p$ of the Hilbert space h. One can make explicit the orthogonal projections

$$f \in H \longmapsto P^\omega_{a,j} f \in H$$

onto the subspaces $\{f\,;\, R_{a,\theta_j}[f] = g_j\}$ for $j = 1,\ \ldots,\ p$. Therefore the operators $P^\omega_{a,j}$ involved in Kaczmarz's iterative algorithm are given (using (2.5)) as

$$\begin{aligned} P^\omega_{a,j}\, f &= f + \omega R^*_{a,\theta_j} \circ \big[R_{a,\theta_j} \circ R^*_{a,\theta_j}\big]^{-1} \Big(g_j - R_{a,\theta_j}[f]\Big) \\ &= f + \omega\, R^*_{a,\theta_j}\Big(\frac{g_j - R_{a,\theta_j}[f]}{B_{a,\theta_j}}\Big) \\ &= f + \omega\, \overline{\mathrm{A}_{a,\theta_j}} \times \Big(\frac{g_j - R_{a,\theta_j}[f]}{\sqrt{1-s^2}\, B_{a,\theta_j}}\Big)_{s=\langle (x,y)\,,\,\theta_j\rangle} \\ &= f + \omega\, \overline{\mathrm{A}_{a,\theta_j}} \times \Big(\frac{g_j - R_{a,\theta_j}[f]}{R_{\theta_j}\big[|A_{a,\theta_j}|^2\big]}\Big)_{s=\langle (x,y)\,,\,\theta_j\rangle}. \end{aligned}$$

Using the expression of $P^\omega_{a,j}$ in (2.6), Kaczmarz's iterative algorithm in (2.6) can be written explicitly as follows

$$\begin{aligned} & f_{k,0} = f_k, \\ & f_{k,j} = P^\omega_{a,j}\, f_{k,j-1} = f_{k,j-1} + \omega \overline{\mathrm{A}_{a,\theta_j}} \times \Big(\frac{g_j - R_{a,\theta_j}\,[f_{k,j-1}]}{R_{\theta_j}\big[|A_{a,\theta_j}|^2\big]}\Big)_{s=\langle (x,y)\,,\,\theta_j\rangle}\,, \quad 1 \le j \le p \\ & f_{k+1,0} = f_{k,p} \end{aligned} \tag{3.3}$$

starting with an arbitrary initial data $f_0 = f_{0,0}$.

4. Numerical Simulations

In order to test the performances of our algorithm in reconstructing images when the tissue attenuation distribution is completely known, we simulated computer-generated phantoms for both the distribution of the activity f and the tissue attenuation distribution a. We did two numerical experiments with different image-phantoms using both optimal and strongly suboptimal data sampling. The performance of our algorithm in correcting attenuation effects was compared with the conventional ART algorithm. Also we tested the sensitivity of the algorithm to additional Gaussian noise. In order to quantitatively evaluate the results, we included L^2 error estimates and compared profiles through the true activity to the corresponding profiles of the reconstructed images.

4.1. Phantoms

We generated two activity models with MATLAB. The first one, denoted phantom 1 (see Fig. 4.1a) corresponds to the distribution

$$f(x,y) = \mu_1 \chi_{E_1}(x,y) + \mu_2 \chi_{E_2}(x,y) + \mu_3 \chi_{E_3}(x,y)$$

where E_1, E_2, E_3 are characteristic functions of three large ellipses and μ_1, μ_2, μ_3 are given strictly positive constants of approximatively the same size, such that $\mu_i \simeq \mu_j \ i \neq j$. The attenuated projections g_j of such an activity are strongly correlated. Thus the convergence of ART can be seriously slowed. Therefore, this activity model will be used to test the ability of our algorithm to reconstruct slowly varying spatial distributions that may reduce performances of iterative algorithms.

The second one, denoted phantom 2 (see Fig. 4.1b) corresponds to an approximation of

$$f(x,y) = \sum_{k=1}^{M} \nu_k \delta(x - x_k, y - y_k)$$

realized as a linear combination of characteristic functions of small ellipses, the ν_k for $k = 1, \ldots, M$, are random generated positive constants. Such kind of activity model will be used to test the capacities of the algorithm to recover "accidents" and small details in discontinuous activity distributions which may vary in a random way.

In order to perform a realistic model, we took a strongly non uniform tissue attenuation distribution already used in [14]. The image of our phantom of the attenuation tissue distribution (see Fig. 4.1c) across a section of a human body shows an ellipsoidal region with axes of length 22.5 cm and 30 cm. Also Fig. 4.1c shows two smaller disjoint ellipsoidal zones with axes of length respectively 10 and 8.8 cm and two circular disjoint regions of diameter 2.5 cm. The circular and ellipsoidal regions are disjoint. The smaller ellipsoidal zones correspond to lungs, while the circular regions correspond to bones. The attenuation distribution equals to 0.01 cm^{-1} within lungs and to 0.17 cm^{-1} within bones, while it equals 0.15 cm^{-1} within the remainder part of the large ellipse.

In both experiments, all images were given on a $N \times N$ grid with N equals to 128. The SPECT measurements were given by the attenuated Radon transform computed with N_τ projections equispaced between 0 and 2π. Here τ is equal to $360/N_\tau$, where the number N_τ of projections was chosen in order to agree with the optimal sampling condition $N_\tau/N \simeq \pi/2$ given in [15] for transmission tomography using $[0, \ \pi]$ as an angular range. Because of the involvement in our case of some nonzero tissues attenuation distribution, the SPECT measurement

(a) (b) (c)

Fig. 4.1. Model distributions: (a) activity phantom 1; (b) activity phantom 2; (c) attenuation.

are computed from 0 to 2π. Thus the optimal relation between N and N_τ becomes $N_\tau/N \simeq \pi$, which is satisfied taking $N_\tau = 400$ projections into account. Since this ratio falls frequently in practice much below the value π, we included numerical studies from suboptimal numbers of projections corresponding to the ratio $N_\tau/N = \pi/5$. This leads us to take only 80 equispaced projections in consideration.

4.2. Reconstruction

In this section we perform the reconstruction of both phantom 1 and 2 using the algorithm described in (3.3). The tissue attenuation distribution a is chosen as in the section 4.1.

In order to improve the stability of the reconstructed activity distribution, we will correct the solution provided by our algorithm at each iteration taking into account natural constraints which need to be fulfilled by the expected solution. Since we are dealing with the reconstruction of a cross section of human body, a non-negativity constraint is required in order to provide physical meaning to the solution (see [2] for more constraint schemes). Therefore, after each iteration k of the algorithm, the approximated activity distribution f^k which has been found will be replaced by $\sup(f^k, 0)$. It has been shown that the projection access order has an important impact on the convergence rate and the stability of the ART methods. Thus several schemes have been proposed in order to improve both convergence speed and reconstructed image quality (see Intes *et. al* [10] for further details). The goal is to rearrange the measurements in such a way that the projections are closest to perpendicularity. For this end, we chose a random access scheme (see [25]) that gives better results relative to the sequential access scheme. The sequential access scheme is the natural order access. It access to the projections with respect to the order of the acquired experimental data. The relaxation parameter adjusts the projection step at each iteration and its selection is most of the time done empirically. We have set $w = 0.1$ based on a previous studies such in Ros *et. al* [20]. Using iterative algorithms implies that the solution f should be initialized with a constant value or a good start guess. Another common starting guess is $f_0 = f_{0,0} = 0$, which will be chosen for our numerical experiments.

Therefore, in the approach which is conducted here, the algorithm depends on two parameters, namely the step p of orthogonal projections on various subspaces $\{f\,;\, R_{a,\theta_j}\, f = g_j\}$ and the number K of iterations. We performed two tests taking the values $p = 1$ as optimal value using 400 projections and $p = 5$ as suboptimal value using only 80 projections, in order to see how the choice of p, K affects the quality of the reconstruction where $K = 1, \ldots, 30$ for both

values of the parameter p. To quantitatively compare reconstructed activity densities $f^{p,K}$ by our algorithm and the reconstructed activity densities $f_{art}^{p,K}$ by the classical ART with no attenuation correction to the true one f, we define the following relative errors expressed in %

$$E^{p,K} = \frac{\|f - f^{p,K}\|}{\|f\|} * 100 \text{ and } E_{art}^{p,K} = \frac{\|f - f_{art}^{p,K}\|}{\|f\|} * 100$$

where $\|.\|$ is the L^2 norm.

4.2.1. Reconstruction in the case of slowly varying activity

The image displayed in Fig. 4.2a is the reconstructed image of the activity distribution phantom 1 with our algorithm after 10 iterations. Each iteration using a step $p = 1$ of orthogonal projections, that is as many angles as used for the computation of the discrete attenuated Radon transform. Here the corresponding L^2 relative error is $E^{1,10} = 0.54\%$. Fig. 4.2b illustrates the reconstructed image by the classical ART algorithm using the same values for the parameters p and K. The L^2 relative error yielded is $E_{art}^{1,10} = 4.6\%$. The profiles drawn along the horizontal axis $y = 0$ across the phantom 1 and the reconstructed images from both

(a) (b)

Fig. 4.2. Reconstruction of the activity "phantom 1" with $p = 1$ and $K = 10$: (a) reconstructed image $f^{p,K}$; (b) reconstructed image $f_{art}^{p,K}$

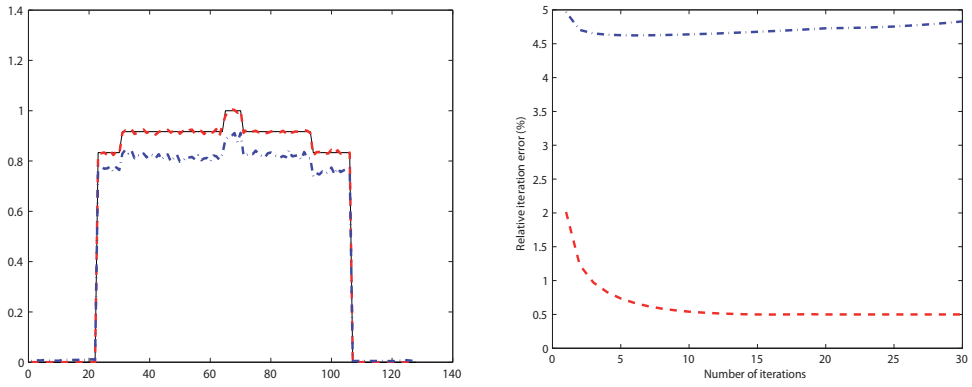

(a) (b)

Fig. 4.3. Comparison results with $p = 1$: (a) profiles of f (solid line) and the reconstructed activity distribution densities : $f^{p,K}$ (dashed line), $f_{art}^{p,K}$ (dash-dotted line) for $y = 0$; (b) L^2 relative error $E^{p,K}$ (dashed line) and $E_{art}^{p,K}$ (dash-dotted line) for $K = 1, \ldots, 30$.

algorithms are shown respectively in Fig. 4.3a, while Fig. 4.3b shows the relative errors $E^{p,K}$ and $E^{p,K}_{art}$ plotted as functions of the number of iterations.

Both L^2 relative error and comparison of profiles show that the reconstructions obtained by the classical ART algorithm without an attenuation correction differ significantly from the original image even under optimal sampling conditions. Moreover, we notice that shadows can be seen in the reconstructed image due to non corrected attenuation effects. On the other hand, the present algorithm yields images which match perfectly the original phantom used in the simulations and shows good stability results for the solutions when the number of iterations increases. Furthermore, the strongly correlated measurements data didn't affect the convergence speed of our algorithm.

Also we conducted simulations when the measurements data suffered from a highly suboptimal ratio of the number between projections and the number of samples. The following numerical experiment was computed taking the value $N_\tau/N \simeq \frac{\pi}{5}$ as a sampling ratio which corresponds to $p = 5$. In this case we have only 80 equispaced projections in the angular range $[0,\ 2\pi]$. Figs. 4.4a and 4.4b show images computed using the present algorithm and the classical ART method respectively after $K = 10$ iterations. L^2 relative error was respectively equal to $E^{1,10} = 2.89\%$ and $E^{1,10}_{art} = 7.5\%$.

In order to make a quantitative comparison, we show the profiles of reconstructions and the true activity distribution , which are both taken across the horizontal axis $y = 0$, in Fig. 4.5a. Furthermore, we display the relative errors $E^{p,K}$ and $E^{p,K}_{art}$ as functions of number of iterations K. In Fig. 4.5b K describes the interval $[1,\ 30]$. As shown in Figs. 4.4 and 4.5, if the reconstruction is done in the presence of strongly varying attenuation distribution and suboptimal sampling ratio,and if we do not correct or compensate the attenuation effect, then in this case the smoothness of solutions will be deteriorated and the relative error of reconstruction will linearly increase as the number of iterations increases. While using the proposed attenuation correction method, it is possible to obtain a good reconstruction with a small relative error and a stable behavior of solutions even in case of high suboptimal sampling ratio. On the other hand, the strongly correlated measurements data do not affect the convergence speed of our algorithm.

4.2.2. Reconstruction in the case of discontinuous activity distribution

In this section we implemented our algorithm starting with "phantom 2" as the activity distribution. Fig. 4.6a features the reconstructed activity distribution $f^{p,K}$ obtained with our algorithm after 10 iterations, each iteration using a step $p = 1$ of orthogonal projections, that is using all possible angles involved for the preliminary computation of the attenuated Radon transform. Here the corresponding L^2 relative error $E^{1,10}$ is here almost equal to 0. Fig. 4.6b shows the reconstructed activity distribution $f^{p,K}_{art}$ obtained with the classical ART algorithm after 10 iterations and with the same step $p = 1$. In this case the relative error obtained is $E^{1,10}_{art} = 5.7\%$. In Fig. 4.7a, we plotted both horizontal profiles taken at the center of the original phantom and the reconstructed images. Fig. 4.7b features the variations of the functions $E^{p,K}$ and $E^{p,K}_{art}$ for K between 1 and 30 and p equals to 1. In this case, $E^{1,K}$ decreases much faster than $E^{1,K}_{art}$. Moreover $E^{1,K}$ asymptotically converges to zero, while $E^{1,K}_{art}$ tends to increase starting from the iteration $K = 20$.

The computational examples of this section prove that using an algorithm, which do not take into account the attenuation correction in the reconstruction of distribution models, suffers of

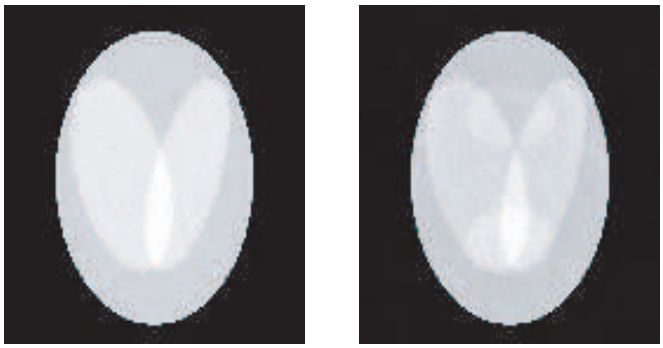

(a) (b)

Fig. 4.4. Reconstruction of the activity "phantom 1" with $p = 5$ and $K = 10$: (a) reconstructed image $f^{p,K}$; (b) reconstructed image $f_{art}^{p,K}$.

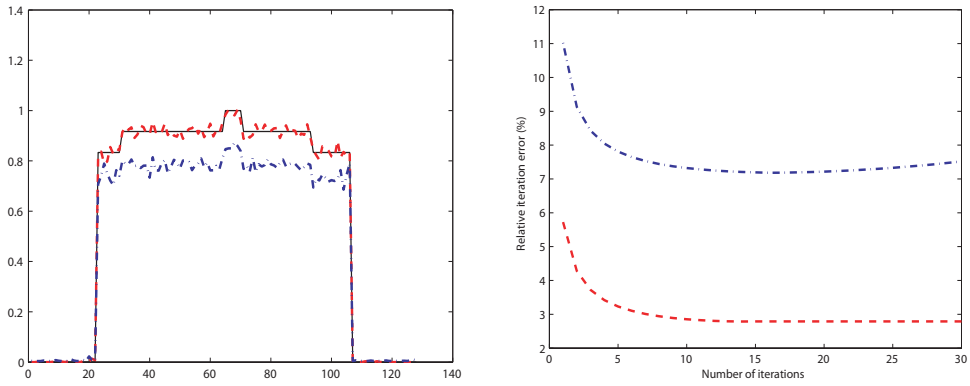

(a) (b)

Fig. 4.5. Comparison results with $p = 5$: (a) profiles of f (solid line) and the reconstructed activity distribution densities : $f^{p,K}$ (dashed line), $f_{art}^{p,K}$ (dash-dotted line) for $y = 0$; L^2 relative error $E^{p,K}$ (dash line) and $E_{art}^{p,K}$ (dash-dotted line) for $K = 1, \ldots, 30$.

lack in accuracy (poor details reconstruction) and loss of activity intensities and brilliance. Also we noticed that oscillations appear in the reconstructed activities when these are yielded by the conventional ART algorithm. This did not happen using our approach. In fact our algorithm provides an exact reconstruction and a perfect contrast quality of phantoms containing fast varying distributions. One can see from the profiles comparison that edges of the details were reproduced accurately and perturbations didn't occur in the reconstructed image.

As in the case of slow varying activity distribution, we performed reconstruction for phantom 2 with suboptimal sampling condition. The simulations displayed in Figs. 4.8 and 4.9 were done by using 80 equispaced projections. For this end, we ran the algorithm setting $p = 5$. The images shown in Figs. 4.8a and 4.8b illustrate the reconstructed activities $f^{p,K}$ and $f_{art}^{p,K}$ respectively after 10 iterations. The corresponding L^2 relatives errors were respectively 4.5% and 22.6%. The profiles taken at the axis $x = 0$ through $f^{p,K}$ and $f_{art}^{p,K}$ are shown in Fig. 4.9a and superimposed with the corresponding profile through the true activity distribution f for comparison. Figure 4.9b shows how $E_{art}^{p,K}$ begins to slightly increase starting from the 19^{th} iteration, while $E^{p,K}$ asymptotically decreases to 1.7%.

As one can see, we obtained impressive results applying our method of reconstruction. Our

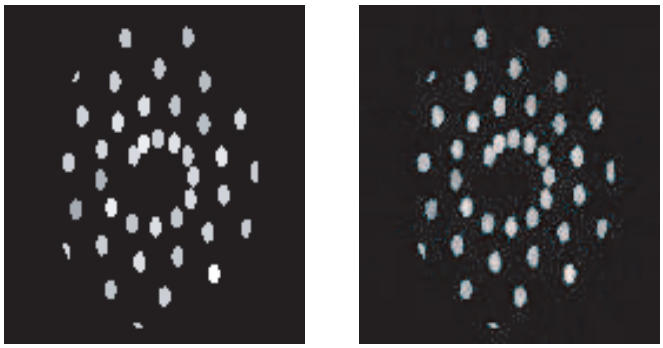

(a) (b)

Fig. 4.6. Reconstruction of the activity "phantom 2" with $p = 1$ and $K = 10$: (a) reconstructed image $f^{p,K}$; (b) reconstructed image $f_{art}^{p,K}$.

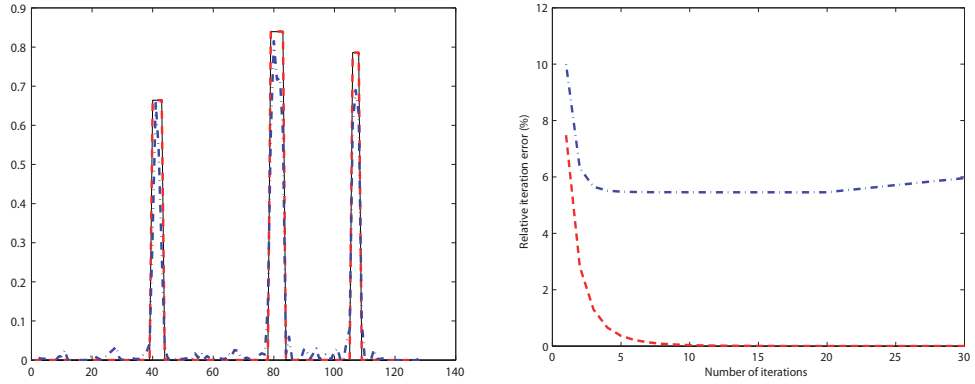

(a) (b)

Fig. 4.7. Comparison results with $p = 1$: (a) profiles of f (solid line) and the reconstructed activity distribution : $f^{p,K}$ (dashed line), $f_{art}^{p,K}$ (dash-dotted line) for $y = 0$; (b) L^2 relative error $E^{p,K}$ (dashed line) and $E_{art}^{p,K}$ (dash-dotted line) for $K = 1, \ldots, 30$.

algorithm displays good stability and accuracy in face of insufficient number of projections since there were no star-like artifacts in the reconstructed images. In fact the star-like artifact is a pronounced phenomenon that appears when both attenuation and suboptimal number of projection are present. Furthermore, all the details of the original phantom were reproduced. On the other hand, and under the same circumstances, the ART algorithm, which do not take into account the attenuation correction, produced low-contrast images that contain an important amount of noise level.

4.3. Reconstruction from noisy data

We conclude our presentation by the reconstruction of the "Shepp-Logan" phantom (see Fig. 4.10a) from noisy data. The Shepp-Logan phantom includes several fine objects with multiple intensity levels (details with discontinuous geometry) and also large smooth areas. Thus such an activity distribution simulates realistic models, so we used it to measure how the noisy data affects the reconstruction in terms of spatial resolution and image contrast. At first time. First the SPECT measurements were calculated by the attenuated radon transform using the same attenuation distribution described in the previous section. Then in order to generate noisy

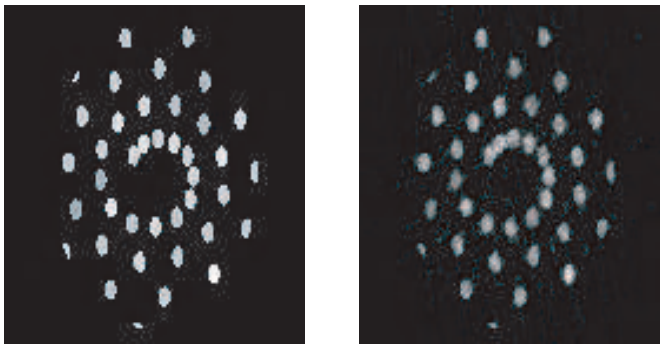

(a) (b)

Fig. 4.8. Reconstruction of the activity "phantom 2" with $p = 5$ and $K = 10$: (a) reconstructed image $f^{p,K}$; (b) reconstructed image $f_{art}^{p,K}$.

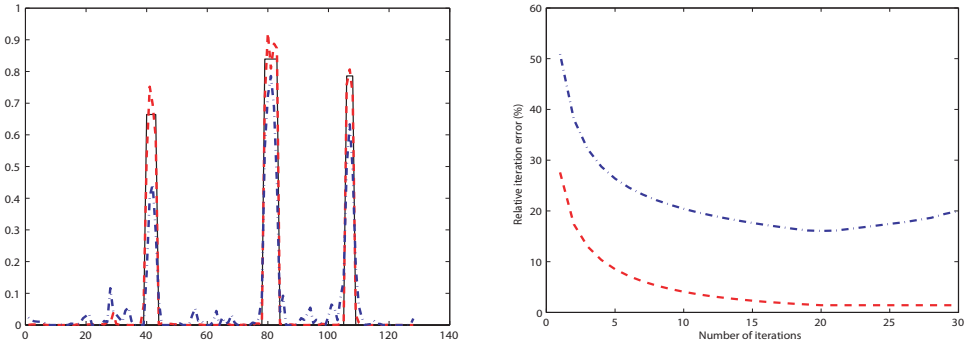

(a) (b)

Fig. 4.9. Comparison results with $p = 5$: (a) profiles of f (solid line) and the reconstructed activity distribution : $f^{p,K}$ (dashed line), $f_{art}^{p,K}$ (dash-dotted line) for $y = 0$; L^2 relative error $E^{p,K}$ (dashed line) and $E_{art}^{p,K}$ (dash-dotted line) for $K = 1, \ldots, 30$.

data, we added Gaussian noise with an average equals 0 and a deviance σ^2 equals 0.1 to each projection. The resulting data had a relative mean square error of 12%. In order to satisfy practical conditions such the suboptimal sampling, we ran our algorithm with the noisy data setting $p = 5$.

The image displayed in Fig. 4.10b was computed using the present algorithm without additional filtration and after $K = 10$ iterations. Image in Fig. 4.10c was obtained using our method with an application of a low-frequency filtration procedure. The filtered version of our algorithm consists of two steps. At each iteration, we filtered the projections g_j for $j = 1, \ldots, 80$ with the low-frequency filter $\hat{W}(\rho)$ given by

$$\hat{W}(\rho) = \begin{cases} \frac{1}{2}(1 + \cos(\pi\rho/\rho^{\text{cut-off}})) & |\rho| \leq \rho^{\text{cut-off}} \\ 0 & |\rho| > \rho^{\text{cut-off}}. \end{cases}$$

where $\rho^{\text{cut-off}}$ is the cut-off frequency, $\rho^{\text{cut-off}} \leq \rho^{\text{Nyquist}}$. Then after each full iteration, the image $f^{p,k}$ is filtered using a 2-D median filter. Thus spikes from reconstruction noise are removed without blurring the edges. Analyzing images presented in Fig. 4.10 one can observe that the low-frequency filtration reduces oscillations in the reconstructed image with a moderate loss of fine details.

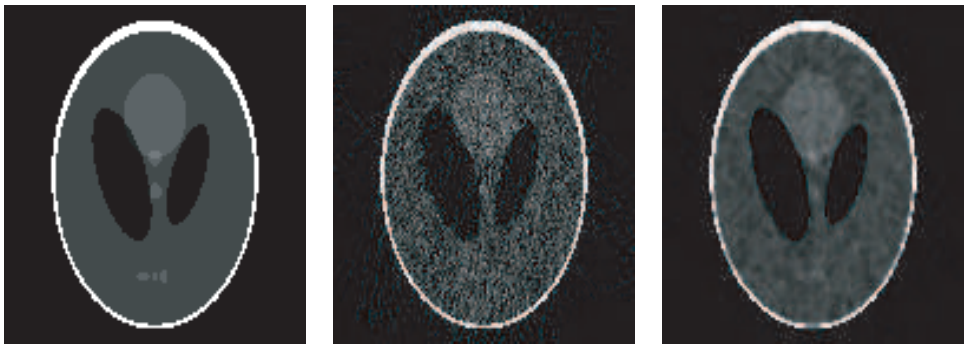

(a) (b) (c)

Fig. 4.10. Reconstruction of phantom "Shepp-Logan" from noisy data : (a) original phantom ; (b) reconstruction without filtering ; (c) reconstruction with filtering.

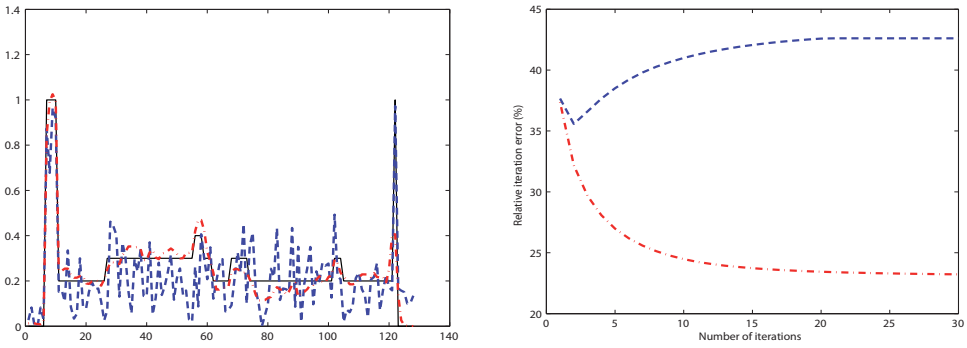

(a) (b)

Fig. 4.11. Comparison results : (a) profiles of f (solid line), reconstructed activity without filtering (dashed line) and reconstructed activity with filtering (dash-dotted line) for $x = 0$; (b) L^2 relative error evolution: without filtering (dashed line) and with filtering (dash-dotted line) for $K = 1, \ldots, 30$.

In order to visualize how the filtration step modifies our algorithm behavior in term of the reconstruction quality and the L^2 relative error, we plotted profiles taken at the vertical axis $x = 0$ across the phantom and the reconstructed images in Fig. 4.11a and we displayed $E^{p,K}$ as a function of K for $K = 1, \ldots, 30$ in Fig. 4.11b. One can see from the graphs comparison that the filtering procedure of our algorithm greatly improves the quality of reconstruction and significantly reduces oscillations, while the relative error analysis shows a diverging behavior of our method. On the other hand, when the reconstruction is done with the filtered version of our algorithm, stable solutions occur and convergence is established.

5. Conclusion and Discussion

This paper presents a method to reconstruct emission activity by an algorithm incorporating implicit and exact attenuation correction. We investigated the impact of the attenuation effects, strongly correlated projections and insufficient measurements in our reconstruction approach.

The computer simulations show that the present method can indeed be used to improve reconstructed images quality in case the of realistic arbitrary attenuation maps and gives better results than the classical ART. The present algorithm displays an accuracy in reconstructing

images that contain small details even when the data measurements suffer from high suboptimal sampling. Since our algorithm need a small number of projections for accurate reconstruction, then less computational time is required.

On the other hand, a strong correlated set of projections due to a slow varying activity distribution seems to be controlled by our algorithm as it was shown by the L^2 error estimate studies.

The filtered version algorithm seems to handle oscillation problems when facing moderately noisy data. We should note that it is possible to apply the present algorithm to real data, however, there is a need for further investigation to increase numeric robustness. There should be more investigations as well in both adapted filtering methods and finding the optimal choice of relaxation parameters.

In our first approach, angles used for the reconstruction were regularly organized within $[0, 2\pi[$. Nevertheless, our routine allows the possibility of choosing an arbitrary set of angles, introducing for example some gaps in the list of selected angles. Since our approach will allow us to avoid angular sectors in which the attenuation takes an important role in the projections, it will be useful to accomplish studies on the reconstruction of the unknown source only when we dispose of partial information about the attenuation map.

Acknowledgments. The author is grateful to A. Yger for encouragement and many helpful discussions.

References

[1] W. Backfrieder, S. Bekner, G. Engelbrecht, Web-based parallel ML-EM reconstruction for SPECT and SMP clusters, *Proceedings of the international conference on mathematics and engineering techniques in medicine and biological sciences*, Las Vegas, Nevada, USA, (2001), 25-28, CESERA Press.

[2] Y. Censor, Finite series-expansion reconstruction methods, *Proc. IEEE*, **71** (1983), 409-419.

[3] L.T. Chang, A method for attenuation correction in radionuclide computed tomography, *IEEE T. Nucl. Sci.*, **25** (1987), 638-643.

[4] Y-W. Chen, Z. Nakao, S.Tamura, Attenuation correction for X-Ray emission computed tomography of laser-produced plasma, *IEICE*, **E79-A** (1995), 1287-1290.

[5] A.P. Dempster, N.M. Laird and D.B. Rubin, Maximum likelihood from incomplete data via the EM algorithm, *J. Roy. Stat. Soc.*, **39** (1977), 1-38.

[6] R. Gordon and G. T. Herman, Reconstruction of pictures from their projections, *Commun. Assoc. Comput. Mach.*, **14** (1971), 759-768.

[7] R. Gordon, R. Bender and G. T. Herman, Algebraic reconstruction techniques (ART) for three-dimensional electron microscopy and X-ray photography, *J. Theor. Biol.*, **29** (1970), 471-481.

[8] G.T. Herman and L.B. Meyer, Algebraic reconstruction techniques can be made computationally efficient, *IEEE T. Med. Imaging*, **12** (1993), 600-609.

[9] H.M Hudson, R.S. Larkin, Accelerated image reconstruction using ordered subsets of projection data, *IEEE T. Med. Imaging*, **13** (1994) 601-609.

[10] X. Intes, V. Ntziachristos, J. P. Culver, A. Yodh and B. Chance, Projection access order in algebraic reconstruction technique for diffuse optical tomography, *Phys. Med. Biol.*, **47** (2002), N1-N10.

[11] S. Kaczmarz, Angenährte Auflösung von Systemen hearer Gleichungen, *Bull. Int. Acad. Pol. Sci. Lett. A*, **35** (1937), 355-357.

[12] A.C Kak and M. Slaney, Principles of Computerized Tomography, IEEE Press, 1992.

[13] L.A. Kunyansky, New SPECT reconstruction algorithm based on the Novikov explicit inversion formula, *Inverse Probl.*, **17** (2001), 293-306.

[14] S.H. Manglos, R.I. Jaszczak, C.E. Floyd, L.J. Hahn, K.L. Greer and R.E. Coleman, Nonisotropic attenuation in SPECT: phantom tests of quantitative effects and compensation techniques, *J. Nucl. Med.*, **28** (1987), 1584-1591.

[15] F. Natterer, The Mathematics of Computerized Tomography, New York, Wiley-Teunber, 1986.

[16] F. Natterer, Inversion of the attenuated Radon transform Inverse Problems, *Inverse Probl.*, **17** (2000), 113-119.

[17] R.G. Novikov, An inversion formula for the attenuated X-ray transformation, *Ark. Mat.*, **40** (2002), 145-167.

[18] T. Quinto, An introduction to X-ray tomography and Radon transforms, *Proc. Sympos. Appl. Math.*, **63** (2006), 1-23.

[19] R. Ramlau, R. Clackdoyle, Accurate attenuation correction in SPECT imaging using optimization of bilinear functions and assuming an unknown spatially-varying attenuation distribution, *IEEE Nuclear Science Symposium*, **3** (1998), 1684-1688.

[20] D. Ros, C. Falcón, I. Juvells and J. Pavía, The influence of a relaxation parameter on SPECT iterative reconstruction algorithms, *Phys. Med. Biol.*, **41** (1996), 925-937.

[21] L.A. Shepp and Y. Vardi, Maximum likelihood reconstruction in Positron emission tomography, *IEEE T. Med. Imaging.*, **1** (1982), 113-122.

[22] K. Tanabe, Projection method for solving a singular system, *Numer. Math.*, **17** (1971), 203-214.

[23] O.J. Tretiak and C. Metz, The exponential Radon transform, *SIAM. J. Appl. Math.*, **39** (1980), 341-354.

[24] B.M.W. Tsui, G.T. Gullberg, E.R. Edgerton, J. G. Ballard, J. R. Perry, W.H. McCartney and J. Berg, Correction of nonuniform attenuation in cardiac SPECT imaging, *J. Nucl. Med.*, **30** (1989), 497-507.

[25] M. Van Dijk, Iterative Methods in Image Reconstruction, Ph.D. Thesis, Ultrecht Univ., The Netherlands, 1992.